

# Estimation for iron contamination in Si solar cell by ideality factor: Deep neural network approach

Oleg Olikh  | Oleg Lozitsky  | Oleksii Zavorodnii 

Taras Shevchenko National University of Kyiv,  
Kyiv, Ukraine

## Correspondence

Oleg Olikh, Taras Shevchenko National  
University of Kyiv, 64/13, Volodymyrska  
Street, Kyiv, 01601, Ukraine.  
Email: olegolikh@knu.ua

## Funding information

National Research Foundation of Ukraine,  
Grant/Award Number: 2020.02/0036

## Abstract

Defect-assisted recombination often restricts the performance of photovoltaic devices, and in order to mass-produce reliable solar cells, low-cost express methods are in demand, which could monitor contamination during the process of manufacture. In our work, we applied the deep learning-based approach for estimating iron concentration in silicon solar cells by using ideality factor. The simulation of solar cells with the back surface field design for generating labeled training and test datasets was performed using SCAPS-1D software. Our results demonstrate that deep neural networks can predict iron concentration using the ideality factor, temperature, base-thickness, and doping level of solar cells. Our simulation showed smaller prediction errors at high doping level, low temperature, and the two values of ideality factor: the first one for structures containing only iron interstitial atoms and the second for structures where Fe<sub>i</sub> and iron–boron pairs coexist. The proposed method was tested on real silicon structures.

## KEYWORDS

ideality factor, iron contamination, machine learning,  $n^+ - p - p^+$  structure, SCAPS, silicon

## 1 | INTRODUCTION

Metal contamination control remains an important challenge for silicon processing in microelectronics, logic technologies, and manufacture of solar cells (SCs).<sup>1–4</sup> Typically, metal-related defects are characterised by Fourier-transform infrared spectroscopy, electron-paramagnetic resonance, minority carrier lifetime measurements, deep level transient spectroscopy (DLTS), Laplace DLTS, and so forth.<sup>5–7</sup> However, these techniques are time-consuming and require special equipment or/and specially prepared samples. At the same time, the rapid standard SC characterization technique widely used in industry today is current-voltage (IV) measurements. IV characteristics contain important information about electrically active defects.<sup>5,8</sup> Researchers propose several methods based on IV characteristics to diagnose the defects<sup>5,8–11</sup> and consider temperature dependencies of current components<sup>10,11</sup> or IV differential parameters.<sup>8,9</sup> These methods, however, require numerous IV measurements (in the first case) or IV measurements of high accuracy (in the second case).

In our previous work,<sup>12</sup> we show that iron concentration ( $N_{\text{Fe}}$ ) can be estimated by using SC ideality factor ( $n$ ), which is used quite often to characterize semiconductor barrier structures of different types.<sup>13–17</sup> However, the defect signatures are convoluted in the ideality factor with the signatures from many other physical processes. As a result, the analytically obtained expressions for  $N_{\text{Fe}} = f(n)$  are not universal and numerous grading curves have to be used to determine  $N_{\text{Fe}}$ ; moreover, IV must be measured in a range of temperatures.<sup>12</sup>

Over the last decade, various fields of theoretical and applied physics have successfully been solving different problems which do not involve rigid algorithmization by using deep learning methods.<sup>18–20</sup> Moreover, the authors claim<sup>19</sup> that materials informatics (combination of material property calculations/measurements and algorithms of informatics) has become the fourth (along with theory, simulations and experiments) paradigm of science. In our work too, we apply deep learning for predicting iron concentration from the ideality factor (so to say “deep learning for deep levels”). Unlike in

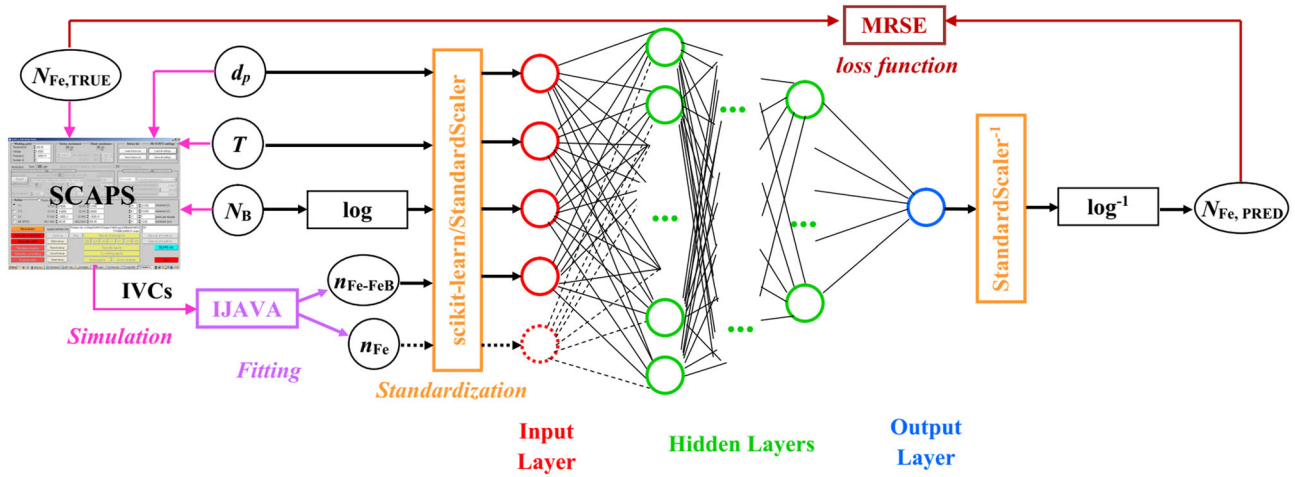


**FIGURE 1** Scheme of deep learning-based approach for predicting iron concentration. Additional details are discussed in the body of the article [Colour figure can be viewed at [wileyonlinelibrary.com](http://wileyonlinelibrary.com)]

Olikh,<sup>12</sup> we applied it to  $n^+-p-p^+$  structure with back surface field (BSF) and took into account the influence of the base thickness on the ideality factor.

In our work, we consider a rather simple system that consists of crystalline silicon (c-Si) SC and iron impurity. Despite its simplicity, the system is important for practical applications since silicon solar cells constitute 90% of current global production capacity<sup>21</sup> and BSF is one of the popular designs that have been used in mass-production of c-Si SCs up to now.<sup>22,23</sup> Surely, the passivated emitter and rear cell technology has recently come to the fore, but PERC solar cells also contain  $n^+-p$  junction and local  $n^+-p-p^+$  junction.<sup>23,24</sup> Iron in these structures is the main and one of the most detrimental metallic impurities.<sup>2-4</sup> The flowchart of the heuristic approach we used is

## 2 | SIMULATION DETAILS

The  $n^+-p-p^+$  structure used in calculations had 0.5- $\mu\text{m}$ -thick emitter layer  $n^+$  with donor concentration  $N_D = 10^{19} \text{ cm}^{-3}$ ; the  $p$ -layer and  $p^+$ -layer were uniformly doped with boron; the base  $p$  had the thickness  $d_p = 150\text{--}240 \text{ }\mu\text{m}$  and dopant concentration  $N_B = 10^{15}\text{--}10^{17} \text{ cm}^{-3}$ ; the BSF-layer  $p^+$  had the thickness  $d_{BSF} (1 \text{ }\mu\text{m})$  and the acceptor concentration  $N_{BSF} = 5 \times 10^{18} \text{ cm}^{-3}$ .

The simulations were carried out over the temperature range 290 – 340 K. For each temperature, the SCAPS setting file was created by using the following material parameters. The bandgap  $E_G$  and bandgap narrowing  $\Delta E_G$  models were taken from Pässler<sup>33</sup> and Yan and Cuevas<sup>34</sup> respectively:

$$E_G = E_{G0} - \alpha\theta \left\{ \frac{1-3\Delta^2}{e^\theta - 1} + \frac{3\Delta^2}{2} \left( \sqrt[6]{1 + \frac{\pi^2}{3(1+\Delta^2)} \left( \frac{2T}{\theta} \right)^2} + \frac{3\Delta^2 - 1}{4} \left( \frac{2T}{\theta} \right)^3 + \frac{8}{3} \left( \frac{2T}{\theta} \right)^4 + \left( \frac{2T}{\theta} \right)^6 - 1 \right) \right\}, \quad (1)$$

shown in Figure 1 where the following steps can be distinguished. First, the dark IV characteristics were simulated for SCs with varied parameters and known contaminant composition. In our numerical simulation, we applied SCAPS-1D<sup>25,26</sup> widely used to model solar cells.<sup>27-32</sup> Second, the obtained IV curves were fitted according to the double-diode model, and the ideality factors were estimated. In the result, the labeled datasets were produced. Obviously, the labeled dataset from experimental IVs would be preferable, but in practice, it is almost impossible to find thousands of samples with the required parameters. Third, the deep neural network (DNN) was trained to estimate iron contamination by using SC's base thickness, doping level, temperature and the ideality factor. Fourth, the DNN was tested by using both synthetic and experimental IV curves.

$$\Delta E_G = 4.20 \times 10^{-5} \left[ \ln \left( \frac{N_D}{10^{14}} \right) \right]^3; \quad \Delta E_G = 4.72 \times 10^{-5} \left[ \ln \left( \frac{N_{B,BSF}}{10^{14}} \right) \right]^3, \quad (2)$$

where  $E_{G0} = 1.1701 \text{ eV}$ ,  $\alpha = 3.23 \times 10^{-4} \text{ eV/K}$ ,  $\theta = 446 \text{ K}$ ,  $\Delta = 0.51$ . The carrier thermal velocities were calculated from the model suggested by Green<sup>35</sup>:

$$v_{th,n} = \sqrt{\frac{8qkT}{0.28m_0\pi}}; \quad v_{th,p} = \sqrt{\frac{8qkT}{0.41m_0\pi}}, \quad (3)$$

where  $m_0$  is a free electron mass. The effective state density masses in the conduction band  $m_{dC}^*$  and valence band  $m_{dV}^*$  were calculated according to the model from Couderc et al.<sup>36</sup>

$$\left(\frac{m_{dC}^*}{m_0}\right)^{1.5} = 1.094 - 1.312 \times 10^{-5}T + 6.753 \times 10^{-7}T^2 + 4.609 \times 10^{-10}T^3, \quad (4)$$

$$\left(\frac{m_{dV}^*}{m_0}\right)^{1.5} = 0.3426 + 3.376 \times 10^{-3}T - 4.689 \times 10^{-6}T^2 + 2.525 \times 10^{-9}T^3. \quad (5)$$

The carrier mobilities and the free carrier effective masses were taken from Klaassen<sup>37</sup> and O'Mara et al.,<sup>38</sup> respectively. The temperature and doping dependencies of Auger recombination coefficients were calculated from models by Altermatt et al.<sup>39</sup>:

$$C_p(T) = (7.91 \times 10^{-32} - 4.13 \times 10^{-35}T + 3.59 \times 10^{-37}T^2) \times \left(1 + (564812T^{-1.6545} - 1) \left(1 - \tanh \left[ \left\{ \frac{p}{5 \times 10^{16}} \right\}^{0.29} \right] \right)\right), \quad (6)$$

$$C_n(T) = 2.8 \times 10^{-31} \times \left(1 + (235548T^{-1.5013} - 1) \left(1 - \tanh \left[ \left\{ \frac{n}{5 \times 10^{16}} \right\}^{0.34} \right] \right)\right). \quad (7)$$

The band-to-band radiation recombination coefficient was taken from Nguyen et al.<sup>40</sup>

The outside surface recombination with electron and hole velocities  $10^3$  cm/s were taken into account. For metal contacts on the rear and front surfaces, the flat bands' conditions were assumed.

The simulations were carried out under the assumption that defect-assisted recombination corresponds only to iron-related deep levels. As the base and BSF-layer are uniform contaminants, iron is assumed to be in concentration  $N_{Fe} = 10^{10} - 10^{13}$  cm<sup>-3</sup>. It is known that Fe in silicon can be in two states: in the form of FeB pair or in the interstitial state Fe<sub>i</sub>. At near room temperature and boron concentration  $>10^{14}$  cm<sup>-3</sup>, almost all Fe bound in FeB pairs is in equilibrium.<sup>41-44</sup> According to Wijaranakula,<sup>44</sup> the concentration of interstitial iron atoms  $N_{Fe_i}$  which remain unpaired in equilibrium state depend on temperature, doping level, and Fermi level  $F$  position. The estimations show that at 340 K,  $N_{Fe_i} \simeq 0.1N_{Fe}$  for  $N_B \simeq 10^{15}$  cm<sup>-3</sup> in the quasi-neutral region of SC base. However, numerous researches show that temporarily dissociation of pairs can be performed either by heating to the temperature above 200°C, or by applying intense illumination at room temperature.<sup>41,42</sup>

The simulations were performed for the following two cases. In the first case, the concentration of totally dissolved iron was given by a sum of concentrations of interstitial iron atoms Fe<sub>i</sub> and trigonal iron-boron pairs Fe<sub>i</sub>B<sub>s</sub>:

$$N_{Fe} = N_{Fe_i} + N_{Fe_iB_s}. \quad (8)$$

The defect distributions in base and  $p^+$ -layer are inhomogeneous, depend on the Fermi level  $F$  position, and are given by<sup>44,45</sup>

$$\frac{N_{FeB}}{N_{Fe}} = \frac{N_B 10^{-23} \exp(-\frac{E_b}{kT})}{\left[1 + \frac{N_b}{10^{18}} \exp(-\frac{E_b}{kT})\right] \left[1 + \exp(-\frac{F-E_{Fe_i}}{kT})\right]}, \quad N_{Fe_i} = N_{Fe} - N_{FeB}, \quad (9)$$

where  $E_b = 0.582$  eV is the binding energy of Fe<sub>i</sub>B<sub>s</sub> pairs,  $E_{Fe_i}$  is the donor level associated with Fe<sub>i</sub>. This case corresponds to the equilibrium condition and in this article it will be referred to as "Fe-FeB."

In the second case, Fe<sub>i</sub> was assumed to be homogeneously distributed ( $N_{Fe_i} = N_{Fe}$ ). This condition can be realized by heat treatment (210°C, 3 min)<sup>46</sup> or intense illumination.<sup>47</sup> This case will be referred to as "Fe."

The donor level  $E_{Fe_i} = E_V + 0.394$  eV with electron  $\sigma_{n,Fe} = 3.47 \times 10^{-11} T^{-1.48}$  cm<sup>2</sup> and hole  $\sigma_{p,Fe} = 4.54 \times 10^{-16} \exp(-\frac{0.05}{kT})$  cm<sup>2</sup> capture cross-sections<sup>45,48</sup> was associated with Fe<sub>i</sub> in our simulations. For Fe<sub>i</sub>B<sub>s</sub> the donor level  $E_{FeB}^D = E_V + 0.10$  eV,  $\sigma_{n,FeB}^D = 4 \times 10^{-13}$  cm<sup>2</sup>,  $\sigma_{p,FeB}^D = 2 \times 10^{-14}$  cm<sup>2</sup> and acceptor level  $E_{FeB}^A = E_C - 0.26$  eV,  $\sigma_{n,FeB}^A = 5.1 \times 10^{-9} T^{-2.5}$  cm<sup>2</sup>,  $\sigma_{p,FeB}^A = 3.32 \times 10^{-10} \exp(-\frac{0.262}{kT})$  cm<sup>2</sup><sup>45,48,49</sup> were used.

The dark forward IV characteristics were generated by SCAPS over a voltage range to 0.45 V. According to the two-diode model, the dark SC current is given by<sup>50</sup>

$$I = I_{01} \left[ \exp\left(-\frac{q(V-R_s I)}{kT}\right) - 1 \right] + I_{02} \left[ \exp\left(-\frac{q(V-R_s I)}{nkT}\right) - 1 \right] + \frac{V-R_s I}{R_{sh}}, \quad (10)$$

where  $I_{01}$  and  $I_{02}$  are saturation currents,  $R_{sh}$  and  $R_s$  are shunt and series resistances. The two-diode model is often applied to describe real Si SCs: in Equation (10) the first diode represents the "ideal" diode and the first term in the equation describes recombination in the base depth and emitter, including their surfaces; the second diode is the so-called recombination diode and the second term describes recombination within the depletion region.<sup>50</sup> The simulated data were fitted by Equation (10) with  $n$ ,  $I_{01}$ ,  $I_{02}$ ,  $R_{sh}$ , and  $R_s$  as fitting parameters. The fitting was performed by meta-heuristic method IJAVA.<sup>51</sup> The typical example of IV curves and fitting results is shown in Supplementary Material. It should be noted that i) the influence of both  $R_s$  (obtained values  $<10^{-2} \Omega$ ) and  $R_{sh}$  (obtained values  $>10^{18} \Omega$ ) can be neglected in the simulated IVs; ii) the contribution of recombination diode current is essential at low bias only and the voltage range (0 – 0.45) V is quite sufficient to determine the ideality factor values accurately.

In our further calculations we used the ideality factors obtained in Fe-case and Fe-FeB-case which are referred to as  $n_{Fe}$  and  $n_{Fe-FeB}$  hereafter. The typical simulated dependencies of the ideality factor are shown in Figure 2 and in Supplementary Material. The detailed discussion about  $n_{Fe}$  and  $n_{Fe-FeB}$  values are presented elsewhere,<sup>52</sup> however it should be noted that (i)  $n$  can be the same for different values of SC parameters; (ii) dependencies of  $n_{Fe}$  and  $n_{Fe-FeB}$  differ not only in absolute values but also in behavior, although insignificantly.

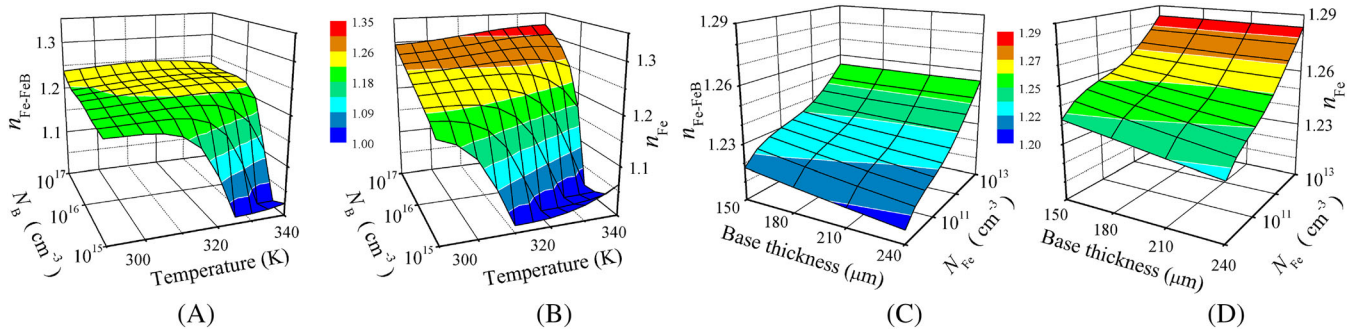


**FIGURE 2** Ideality factor versus temperature and boron concentration (A, B) or base thickness and iron concentration (C, D). The Fe-FeB case (A, C) and Fe case (B, D).  $N_{Fe} = 10^{10} \text{ cm}^{-3}$  (A, B),  $d_p = 180 \text{ μm}$  (A, B),  $N_B = 10^{16} \text{ cm}^{-3}$  (C, D),  $T = 320 \text{ K}$  (C, D) [Colour figure can be viewed at [wileyonlinelibrary.com](http://wileyonlinelibrary.com)]

### 3 | DEEP NEURAL NETWORK MODELS

Deep neural network training requires a large number of samples. In order to build a training dataset, we used IV characteristics simulated by using 4  $d_p$  values, 9  $N_B$  values, 11  $T$  values, and 19  $N_{Fe}$  values, which are regularly distributed (for  $T$  and  $d_p$  in linear scale, for  $N_{Fe}$  and  $N_B$  in logarithmic scale) over the ranges 150–240  $\text{μm}$ ,  $10^{15}$ – $10^{17} \text{ cm}^{-3}$ , 290–340 K, and  $10^{10}$ – $10^{13} \text{ cm}^{-3}$ , respectively. Therefore, 7524 IV characteristics were simulated in Fe case and in Fe-FeB case.

In addition, several test datasets were prepared. For instance, the test dataset labeled “Fe-varied” consists of two subsets. The  $N_{Fe}$  values  $1.300 \times 10^{10}$ ,  $2.471 \times 10^{10}$ ,  $4.696 \times 10^{10}$ ,  $8.927 \times 10^{10}$ ,  $1.697 \times 10^{11}$ ,  $3.225 \times 10^{11}$ ,  $6.130 \times 10^{11}$ ,  $1.165 \times 10^{12}$ ,  $2.214 \times 10^{12}$ ,  $4.209 \times 10^{12}$ ,  $8.000 \times 10^{12} \text{ cm}^{-3}$  (not used during training dataset creation),  $T$  values 290, 295, 300, 305, 310, 315, 320, 325, 330, 335, 340 K (used during training dataset creation),  $d_p$  value 180  $\text{μm}$  (used during training dataset creation), and  $N_B$  values  $1.778 \times 10^{15}$ ,  $5.623 \times 10^{15}$ ,  $10^{16}$ ,  $3.162 \times 10^{16}$ ,  $10^{17} \text{ cm}^{-3}$  (used during training dataset creation) were used to prepare the first subset. Thus, the first subset is based on 605 pairs of IV characteristics. The  $N_{Fe}$  values  $1.200 \times 10^{10}$ ,  $2.234 \times 10^{11}$ ,  $4.160 \times 10^{11}$ ,  $7.746 \times 10^{11}$ ,  $1.442 \times 10^{12}$ ,  $2.685 \times 10^{12}$ , and  $5.000 \times 10^{12} \text{ cm}^{-3}$  (not used during training dataset creation),  $T$  values 290, 300, 310, 320, 330, and 340 K (used during training dataset creation),  $d_p$  values 210 and 240  $\text{μm}$  (used during training dataset creation), and  $N_B$  values  $3.162 \times 10^{15}$ ,  $10^{16}$ , and  $10^{17} \text{ cm}^{-3}$  (used during training dataset creation) were used to prepare the second subset of Fe-varied test dataset. Thus, Fe-varied test dataset is based on  $605 + 252 = 857$  pairs of IV characteristics.

The similar approach was used to prepare “d-varied” (1189 samples), “T-varied” (832 samples), and “B-varied” (514 samples) test datasets. The base thickness, doping level, temperature, and iron concentration values which are different from those in training dataset values were used to prepare “All-varied” dataset (684 samples).

The precise values of parameters are listed in Supplementary Material.

We have tried to construct a DNN that could estimate iron contamination by using SC parameters ( $d_p$  and  $N_B$ ), measured temperatures, and the result of IV fitting (the ideality factor). As shown in Figure 1, two DNNs with different input parameters are under consideration. The input sample of the first DNN consists of  $\{d_p, \log N_B, T, n_{Fe-FeB}\}$ . In practice, this input set can be obtained from one dark IV measurement. This neural network is referred to as DNN<sub>FeFeB</sub> hereafter. The second DNN uses  $\{d_p, \log N_B, T, n_{Fe-FeB}, n_{Fe}\}$  in the input layer. In practice, to obtain a set like this, additional SC processing (e.g., intense illumination) and two IV measurements are required. Further on this neural network is referred to as DNN<sub>FeFeB-Fe</sub>.

The dense deep neural network was implemented through a high-level Keras API provided by TensorFlow.<sup>53</sup> The input layers consist of four or five nodes—see Figure 1. In the output layer, one node and linear activation were used. The five configurations of the hidden layers were considered: (i) “pipe”: each hidden layer contains equal number of nodes; (ii) “trapezium”: six hidden layers, number of neurons linearly decreases from 100% (first layer) to 50% (last layer); (iii) “triangle”: 10 layers, number of neurons linearly decreases from 100% (first layer) to 10% (last layer); (iv) “butterfly”: two serial reflected trapezium configurations; (v) “fir”: two serial trapezium configurations.

The mean squared relative error (MSRE) was chosen as the loss function:

$$\text{MSRE} = \frac{1}{N_s} \sum_{i=1}^{N_s} \frac{(N_{Fe, \text{TRUE}, i} - N_{Fe, \text{PRED}, i})^2}{N_{Fe, \text{TRUE}, i} \cdot N_{Fe, \text{PRED}, i}}, \quad (11)$$

where  $N_s$  is the number of samples in dataset,  $N_{Fe, \text{TRUE}, i}$  is the iron concentration used in the  $i$ th sample simulation, and  $N_{Fe, \text{PRED}, i}$  is the DNN prediction for the  $i$ th sample.

Hyperparameters include the number of nodes for the first hidden layer, the number of hidden layers (in pipe configuration), the batch size, the activation function, the optimizer, the learning rate, the preprocessing method, the dropout rate, the regularization function, the regularization rate, and the weight initializer. The grid search (coarse tuning to limit one hyperparameter) and random search (fine

tuning) were performed over the predefined hyperparameter space shown in Table 1, and the best hyperparameter combination was chosen.

To estimate DNN training, 10-fold cross-validation was used. The performance of the DNN models on test datasets was evaluated by using three metrics: MSRE, coefficient of determination  $R^2$ , and coefficient of correlation  $R$ . Finally, to increase the DNNs performance, a full dataset consisting of training dataset and all the test datasets was used for training of the models.

## 4 | RESULTS AND DISCUSSION

### 4.1 | Synthetic IV curves

The results of hyperparameter search are listed in Table 2. In particular, for  $\text{DNN}_{\text{FeFeB}}$  and  $\text{DNN}_{\text{FeFeB} - \text{Fe}}$ , the trapezium and pipe configurations are chosen, respectively.

The training and test results of  $\text{DNN}_{\text{FeFeB}}$  are presented in Table 3, Table 4, and Figure 3. As seen, MSRE of prediction by  $\text{DNN}_{\text{FeFeB}}$  is sufficiently large. However, it should be noted that in most cases the predictions with big differences between  $N_{\text{Fe, TRUE}, i}$  and  $N_{\text{Fe, PRED}, i}$  are not numerous. In particular, squared relative error (SRE) does not exceed 0.05 for 87%, 88%, and 96% samples in T-varied, d-varied and Fe-varid datasets respectively—see bars in Figure 3. In the case of B-varied dataset (with doping level value non-used in the training dataset), the biggest  $\text{MSRE} = 1.06$  is associated with those not often samples that have a really great SRE ( $>20$ ) while SRE is less than 0.05 for 54% samples. The worst predictions are quite expectedly to be observed for the All-varied dataset:  $R^2$  equals 0.813 and  $\text{SRE} < 0.05$  for only 18% samples. On the other hand, the

Fe-varied dataset is most similar to real situation and the determination and correlation coefficients are high enough (0.991 and 0.996) in this case.

We have also considered the DNN prediction error versus SC parameters—see Figures 4–7. The figures present data for training dataset; The results for test datasets are similar (see Supplementary Material). In particular, Figure 4A shows a considerable increase in prediction error, which is observed at  $T > 320$  K for  $\text{DNN}_{\text{FeFeB}}$ . As seen from Figure 4C, at  $T = 340$  K, the maximum SRE is about 20, and SRE below 0.01 is observed for 55% of the samples whereas these values are equal to 0.02 and 83% at  $T = 290$  K (Figure 4B). It has been shown previously<sup>52</sup> that temperature rise causes the increase in the intrinsic recombination contributions to the ideality factor. As a result, the signature of Shockley-Read-Hall (SRH) recombination in  $n$  value becomes less prominent and DNN predictive ability decreases.

As shown in Figure 5, the SC base thickness practically does not influence the prediction error (the mean value as well as relative frequency). However, as seen from Figure 2C,D, the ideality factor depends on base thickness at constant  $N_{\text{Fe}}$ . Therefore  $d_p$  is a significant parameter for DNN training

The predictive error increases sharply as the doping level decreases—see Figure 6A. In particular, the maximum SRE is about 0.05 for  $N_B = 10^{17} \text{ cm}^{-3}$  (Figure 6C) whereas SRE below 0.05 is only for 56% of samples with  $N_B = 10^{15} \text{ cm}^{-3}$  (Figure 6B). The occupation of holes in Fe-related level determines SRH recombination efficiency. According to the Fermi-Dirac statistics, the probability of hole occupation in a non-degenerate  $p$ -type semiconductor with full acceptor depletion can be expressed as

**TABLE 1** Hyperparameter space for DNNs

| Hyperparameter                 | Values   |
|--------------------------------|--|
| # nodes for first hidden layer | 30, 40, 50, 75, 100, 120, 150  |
| # hidden layers                | 4, 5, 6, 8, 10, 15   |
| batch size                     | 8, 16, 32, 64, 128   |
| activation function            | ReLU, sigmoid, tanh, SELU, ELU   |
| optimizer                      | SGD, RMSprop, Adam, Adadelta, Adagrad, Adamax, Nadam, Ftrl                     |
| learning rate                  | $10^{-5}$ , $10^{-4}$ , $10^{-3}$ , $10^{-2}$                                  |
| # epochs                       | 100, 300, 400, 600, 1000, 1500   |
| preprocessing method           | StandartScaler, MinMaxScaler   |
| regularization function        | None, L2, L1, Dropout  |
| regularization rate            | $10^{-5}$ , $10^{-4}$ , $10^{-3}$ , $10^{-2}$                                  |
| dropout rate                   | 0.2, 0.3, 0.4, 0.5   |
| weight initializer             | Xavier Normal or Uniform, He Normal or Uniform, Random Normal or Uniform, Ones |

**TABLE 2** Chosen hyperparameter combinations

| Hyperparameter            | $\text{DNN}_{\text{FeFeB}}$ | $\text{DNN}_{\text{FeFeB} - \text{Fe}}$ |
|---------------------------|-----------------------------|---|
| # nodes for hidden layers | 120, 108, 96, 84, 72, 60    | 100, 100, 100, 100                      |
| batch size                | 32                          | 32                                      |
| activation function       | ReLU                        | ELU                                     |
| optimizer                 | Adamax                      | Adamax                                  |
| learning rate             | $10^{-3}$                   | $10^{-3}$                               |
| # epochs                  | 400                         | 1500                                    |
| preprocessing method      | StandartScaler              | StandartScaler                          |
| regularization function   | None                        | None                                    |
| weight initializer        | Xavier Normal               | Xavier Normal                           |

**TABLE 3** Results of 10-fold cross-validation

| Dataset  | MSRE                        |   |
|----------|-----------------------------|---|
|          | $\text{DNN}_{\text{FeFeB}}$ | $\text{DNN}_{\text{FeFeB} - \text{Fe}}$ |
| Training | $0.31 \pm 0.07$             | $0.03 \pm 0.01$                         |
| Full     | $0.28 \pm 0.05$             | $0.03 \pm 0.01$                         |



$$f_p = \frac{1}{1 + \frac{N_V}{N_B} \exp\left(\frac{E_V - E_{FeI}}{kT}\right)}. \quad (12)$$

If  $N_B$  decreases, the level is filled with the electron, the SRH recombination stops and the ideality factor value sharply decreases—Figure 2A,B. Moreover, in case of low doping, impurities have only a weak influence on the ideality factor, and therefore, the increase of MSRE is observed. And finally, we believe that the additional factor causing the error to increase at high temperatures is the level filling.

Figure 7A shows that MSRE increases at both low and high iron concentrations. The first  $N_{Fe}$  area of poor DNN accuracy is entirely predictable, the second one seems to be rather surprising. But according to Figure 7C, the MSRE increase is most likely to be due to the fact that only a few samples are predicted with a great SRE at  $N_{Fe} = 10^{13} \text{ cm}^{-3}$  whereas SRE increases more systematically when  $N_{Fe} = 10^{13} \text{ cm}^{-3}$ —Figure 7B.

**TABLE 4** DNN's testing results

| Dataset    | DNN <sub>FeFeB</sub> |       |       | DNN <sub>FeFeB - Fe</sub> |       |       |
|------------|----------------------|-------|-------|---------------------------|-------|-------|
|            | MSRE                 | $R^2$ | $R$   | MSRE                      | $R^2$ | $R$   |
| T-varied   | 0.41                 | 0.936 | 0.967 | 0.020                     | 0.994 | 0.997 |
| d-varied   | 0.37                 | 0.961 | 0.980 | 0.018                     | 0.996 | 0.998 |
| B-varied   | 1.06                 | 0.881 | 0.939 | 0.084                     | 0.991 | 0.995 |
| Fe-varied  | 0.06                 | 0.991 | 0.996 | 0.005                     | 0.999 | 0.999 |
| All-varied | 0.54                 | 0.813 | 0.901 | 0.138                     | 0.948 | 0.974 |

The ideality factor value for the case when only interstitial iron ( $n_{Fe}$ ) is available gives extra information about the defects in comparison with  $n_{Fe - FeB}$ . It is not surprising that DNN<sub>FeFeB - Fe</sub> has better operating parameters compared with DNN<sub>FeFeB</sub>—see Tables 3 and 4 and Figure 8. The predictions improve: MSRE decreases, there is no huge difference between the values of  $N_{Fe, TRUE}$  and  $N_{Fe, PRED}$ , the range of SRE becomes narrow (Figures 4–8). As shown in Figure 8, the maximum SRE does not exceed one even in the case of All-varied dataset, and SRE is below 0.02 for 93%, 92%, 73%, and 97% of the samples in T-varied, d-varied, B-varied, and Fe-varied datasets respectively. It should be noted that for Fe-varied datasets both  $R^2$  and  $R$  are 0.999.

Despite the difference in prediction accuracy, the features of DNN<sub>FeFeB - Fe</sub> and DNN<sub>FeFeB</sub> are similar. Thus, the DNN training with  $N_B$  values, which are expected to be an object of future research, is important for the accuracy of prediction (Figure 8); the increase in the temperature (Figure 4) as well as decrease in doping level (Figure 6) or iron concentration (Figure 7) results in error increase. It should be noted that the prediction error gain with  $N_{Fe}$  increase is not observed in case of DNN<sub>FeFeB - Fe</sub> and the range of SRE at  $N_{Fe} = 10^{13} \text{ cm}^{-3}$  is narrower than that at  $N_{Fe} = 10^{10} \text{ cm}^{-3}$ —see Figure 7B,C.

The results of both DNN<sub>FeFeB</sub> and DNN<sub>FeFeB - Fe</sub> training with a full dataset are presented in Table 3 and Figures 3 and 8F. We can see that in our case, the extension of the labeled dataset practically does not improve the result of DNN. In our opinion, this is an evidence of (i) good DNN configuration tuning; (ii) restricted predictive ability of DNN<sub>FeFeB</sub>, which is caused by ambiguity of dependence  $n_{Fe - FeB} = f(N_{Fe})$ .

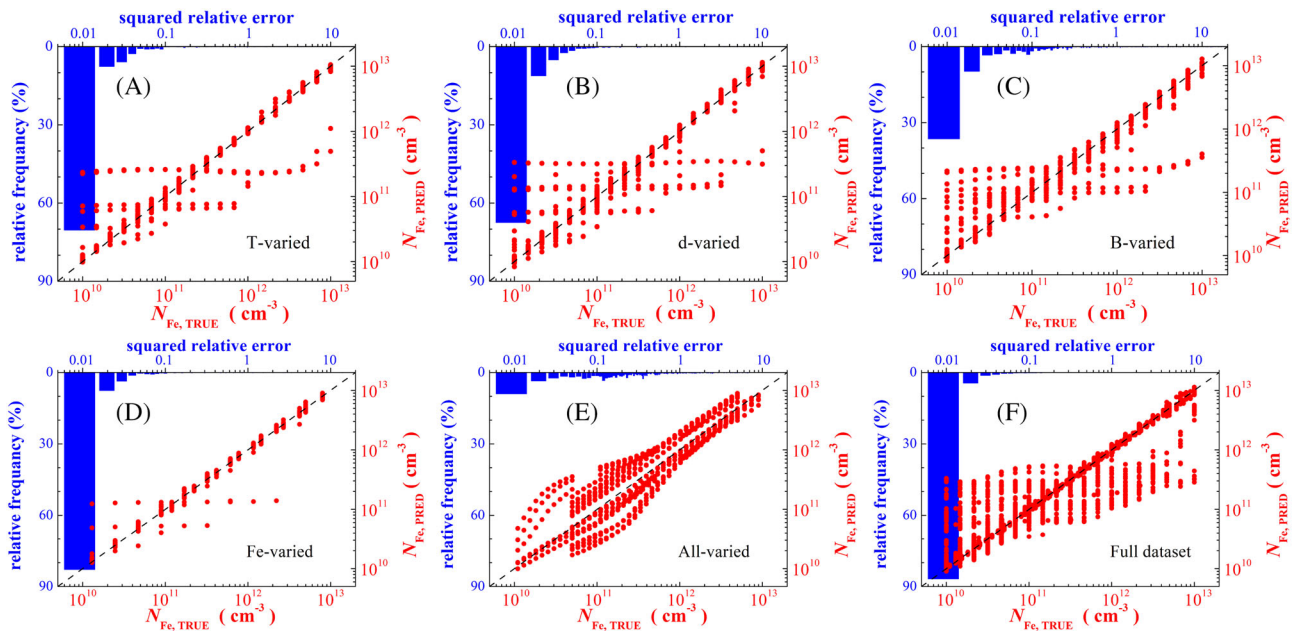


**FIGURE 3** Iron concentrations are plotted against those generated by DNN<sub>FeFeB</sub> on T-varied (A), d-varied (B), B-varied (C), Fe-varied (D), All-varied (E), and full (F) datasets (red points). Bars represent histograms of squared relative error. DNN was learned by training (A)–(E) or full (F) dataset. The black dashed lines are the identity lines serving as the references [Colour figure can be viewed at [wileyonlinelibrary.com](http://wileyonlinelibrary.com)]

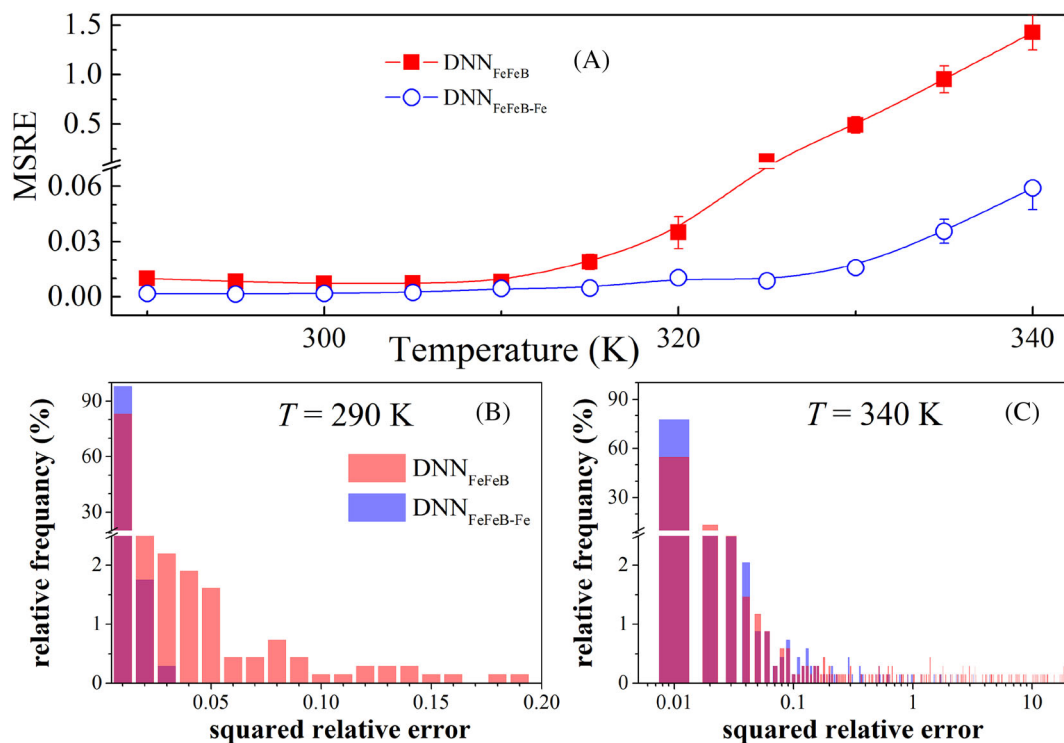


**FIGURE 4** (A) Dependence of the MSRE (training dataset) on the temperature. (B, C) Histograms of squared relative error for  $T = 290$  K and  $T = 340$  K. Red:  $DNN_{FeFeB}$ ; blue:  $DNN_{FeFeB-Fe}$  [Colour figure can be viewed at [wileyonlinelibrary.com](http://wileyonlinelibrary.com)]

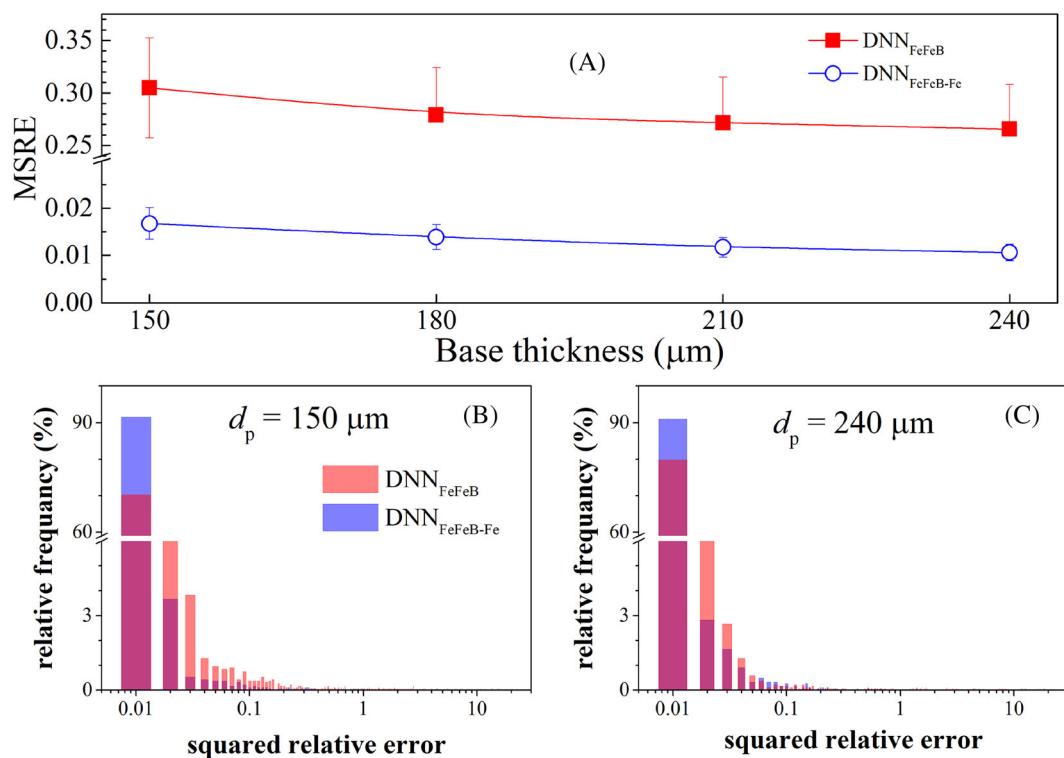


**FIGURE 5** (A) Dependence of the MSRE (training dataset) on the base thickness. (B, C) Histograms of squared relative error for  $d_p = 150$   $\mu m$  and  $d_p = 240$   $\mu m$ . Red:  $DNN_{FeFeB}$ ; blue:  $DNN_{FeFeB-Fe}$  [Colour figure can be viewed at [wileyonlinelibrary.com](http://wileyonlinelibrary.com)]

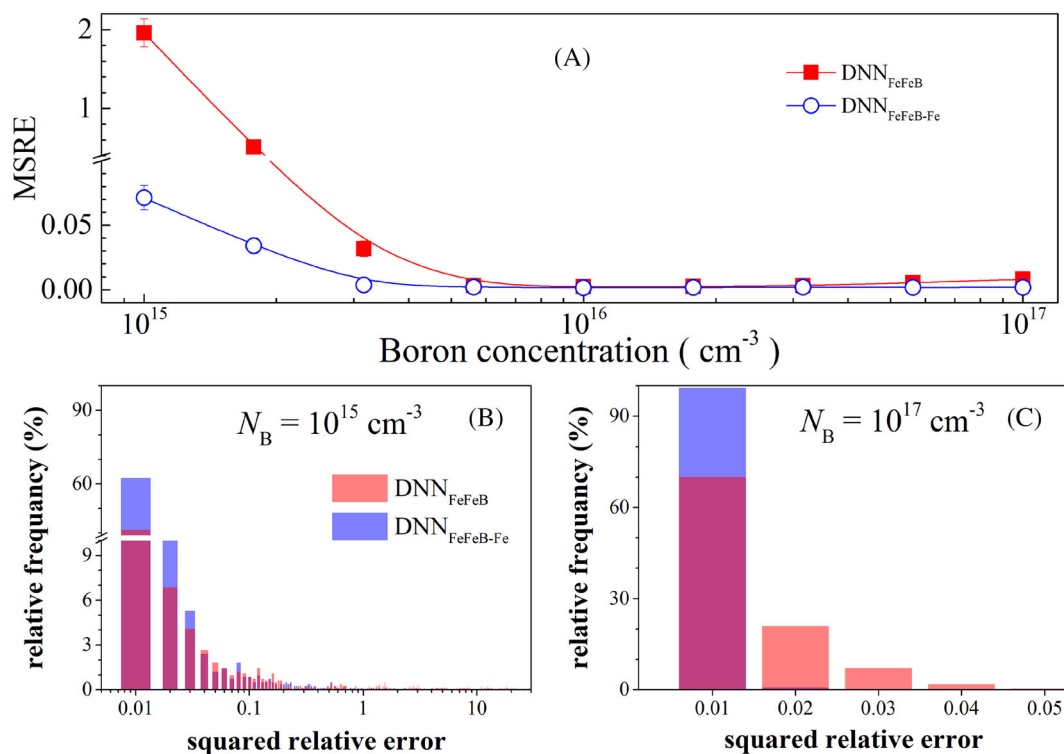


**FIGURE 6** (A) Dependence of the MSRE (training dataset) on the boron concentration. (B, C) Histograms of squared relative error for  $N_B = 10^{15} \text{ cm}^{-3}$  and  $N_B = 10^{17} \text{ cm}^{-3}$ . Red:  $\text{DNN}_{\text{FeFeB}}$ ; blue:  $\text{DNN}_{\text{FeFeB-Fe}}$  [Colour figure can be viewed at [wileyonlinelibrary.com](http://wileyonlinelibrary.com)]

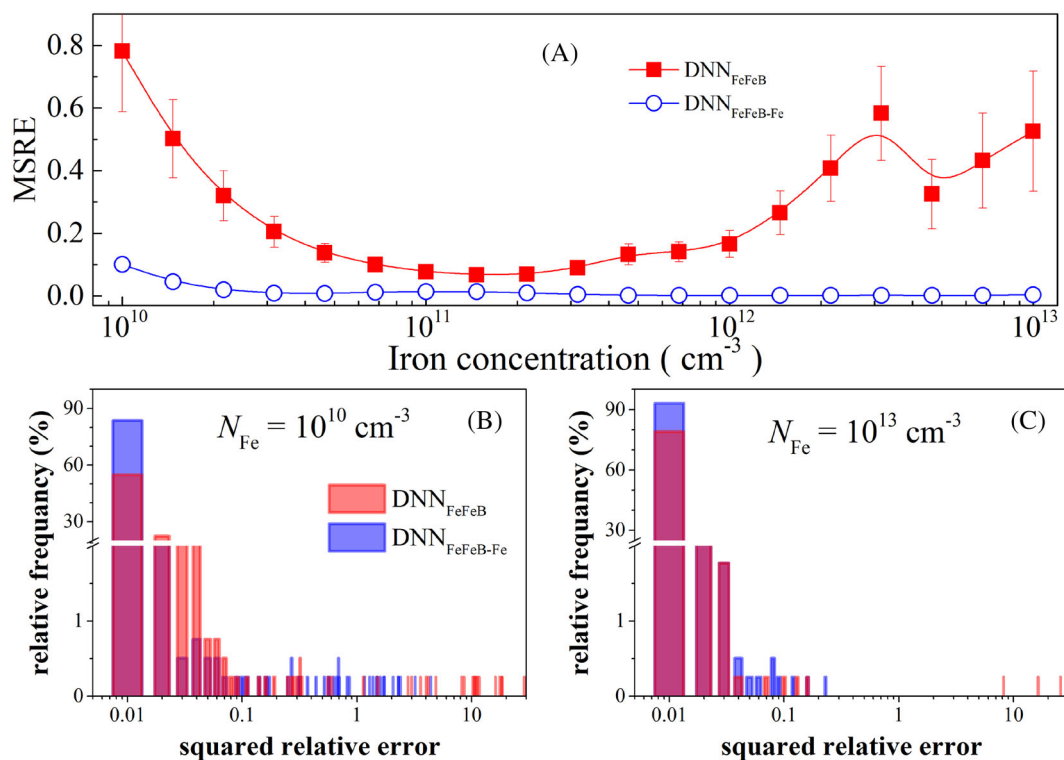


**FIGURE 7** (A) Dependence of the MSRE (training dataset) on the iron concentration. (B, C) Histograms of squared relative error for  $N_{\text{Fe}} = 10^{10} \text{ cm}^{-3}$  and  $N_{\text{Fe}} = 10^{13} \text{ cm}^{-3}$ . Red:  $\text{DNN}_{\text{FeFeB}}$ ; blue:  $\text{DNN}_{\text{FeFeB-Fe}}$  [Colour figure can be viewed at [wileyonlinelibrary.com](http://wileyonlinelibrary.com)]



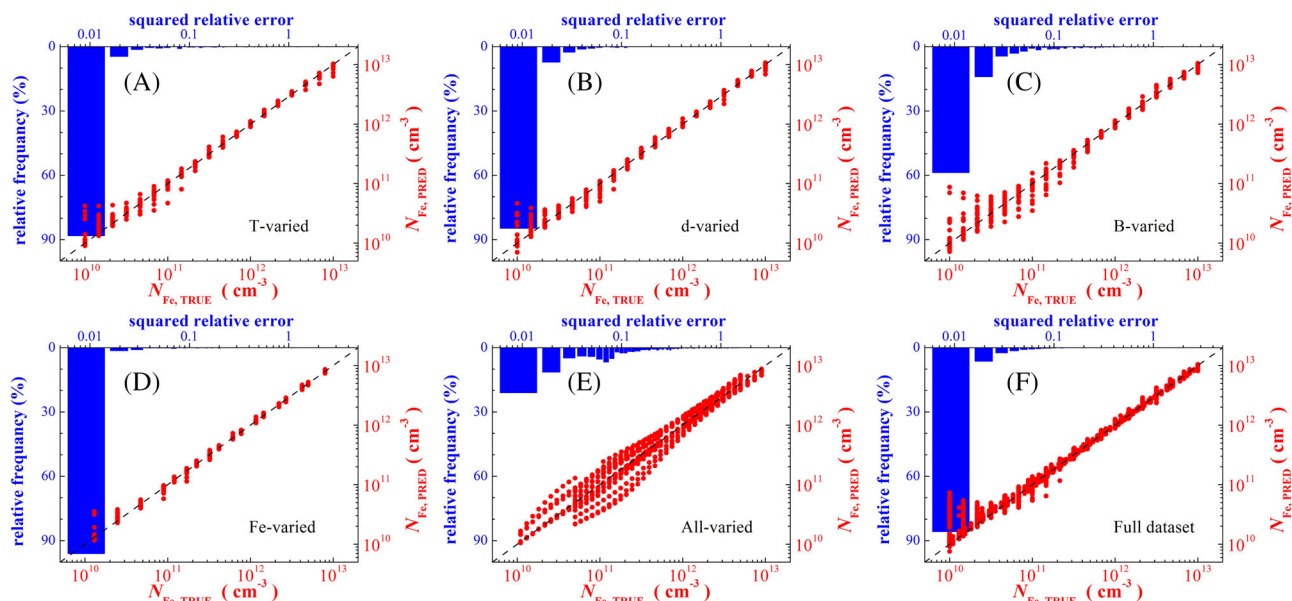


**FIGURE 8** Iron concentrations are plotted against those generated by  $\text{DNN}_{\text{FeFeB}} - \text{Fe}$  on T-varied (A), d-varied (B), B-varied (C), Fe-varied (D), All-varied (E), and full (F) datasets (red points). Bars represent histograms of squared relative error. DNN was learned by training (A)–(E) or full (F) dataset. The black dashed lines are the identify lines serving as the references [Colour figure can be viewed at [wileyonlinelibrary.com](https://onlinelibrary.wiley.com)]

## 4.2 | Experimental IV curves

The ability of DNNs to predict iron concentration in real silicon SCs was tested as well. The samples used in the experiment were  $n^+p$ - $p^+$ -Si structures. The structures were fabricated from  $p$ -type boron-doped Czochralski silicon wafer with [100] orientation and resistivity of 10 Ohm-cm ( $N_B = 1.4 \cdot 10^{15} \text{ cm}^{-3}$ ). The  $n^+$  emitter with sheet resistance of about (20–30)  $\Omega/\square$  and a thickness of 0.7  $\mu\text{m}$  was formed by phosphorus diffusion at 940°C;  $p^+$  layer ((10–20)  $\Omega/\square$ , 0.6  $\mu\text{m}$ ) was formed by boron diffusion at 985°C. The base thickness was 350  $\mu\text{m}$ . The area of the samples was  $1.52 \times 1.535 \text{ cm}^2$ . The concentration of iron in the SC base  $N_{\text{Fe, MEAS}}$  was determined from kinetics of the short circuit current under monochromatic illumination.<sup>54</sup> Two samples used in the investigation are referred to as SC320 and SC349 with  $N_{\text{Fe, MEAS}}$  of  $(2.0 \pm 0.4) \cdot 10^{12} \text{ cm}^{-3}$  and  $(6.7 \pm 0.7) \cdot 10^{12} \text{ cm}^{-3}$ , respectively.

We can see that DNN was faced with a rather difficult task when the complexity was associated with a certain mismatch between the parameters of real structures and those used in the simulation. However, the need for iron-related defects, which predominantly determine recombination, was the main criterion for sampling in our case.

The dark IV characteristics of the samples were measured at temperatures 300, 320, and 340 K. The measurements were carried out after 48 h exposition in the dark at room temperature (“Fe-FeB” case) as well as immediately after intense illumination of the sample with a halogen lamp (“Fe” case). To fit the experimental data and determine fitting parameters, in particular  $n$ ,  $R_s$ ,  $R_{sh}$ , we used Equation (10). The typical results of the measurements and approximations are shown in Figure 9 and Table 5. It should be noted that for real IV curves, in contrast to synthetic ones, the influence of series and shunt resistances

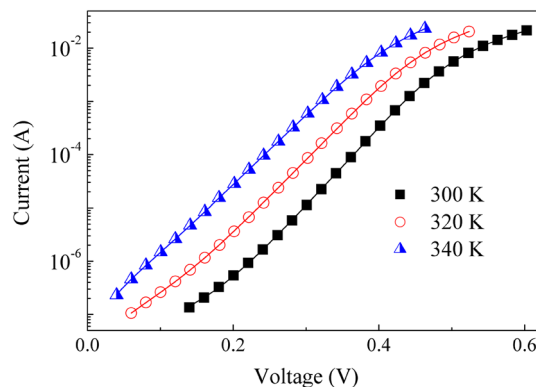


**FIGURE 9**  $I$ - $V$  characteristics measured at 300 K, 320 K, and 340 K for sample SC320. The marks are the experimental results, and the solid lines are the curves fitted by Equation (10) [Colour figure can be viewed at [wileyonlinelibrary.com](https://onlinelibrary.wiley.com)]

cannot be neglected (the magnitude of  $R_s$  is about 3 and 6 Ohm for samples SC320 and SC349, respectively, all the values of  $R_{sh}$  are listed in Table 5).

The ideality factors determined from the experimental curves and the sample parameters were used as input data for  $\text{DNN}_{\text{FeFeB}}$  and  $\text{DNN}_{\text{FeFeB}} - \text{Fe}$ , which were trained either on the training dataset or full dataset. The predictions are listed in Table 5.

First of all, it should be noted that even though we did not use a simulation model of extremely high complexity, the results exceeded our expectations. In particular, the predicted iron concentrations in  $\text{DNN}_{\text{FeFeB}}$  differed only several times from the measured ones. In the case of sample SC320 and  $\text{DNN}_{\text{FeFeB}}$  trained on the full dataset, the error did not exceed 40%.

**TABLE 5** Results of experimental IV fitting and iron contamination testing

| Sample | $N_{\text{Fe, MEAS}}$<br>$10^{12} \text{ cm}^{-3}$ | $T$<br>K | $n_{\text{Fe} - \text{FeB}}$ | $R_{\text{sh, Fe} - \text{FeB}}$<br>Ohm | $n_{\text{Fe}}$ | $R_{\text{sh, Fe}}$<br>Ohm | $N_{\text{Fe, PRED}}, 10^{12} \text{ cm}^{-3}$ |      |   |      |
|--------|--|----------|------------------------------|---|-----------------|----------------------------|--|------|---|------|
|        |  |          |                              |   |                 |                            | $\text{DNN}_{\text{FeFeB}}$                    |      | $\text{DNN}_{\text{FeFeB} - \text{Fe}}$ |      |
|        |  |          |                              |   |                 |                            | training                                       | full | training                                | full |
| SC320  | $2.0 \pm 0.4$                                      | 300      | 1.214                        | $1.6 \cdot 10^6$                        | 1.195           | $1.4 \cdot 10^6$           | 3.9  | 2.8  | 3.0                                     | 2.0  |
|        |  | 320      | 1.204                        | $8.6 \cdot 10^5$                        | 1.148           | $8.0 \cdot 10^5$           | 6.6  | 1.9  | 16                                      | 19   |
|        |  | 340      | 1.118                        | $4.3 \cdot 10^5$                        | 1.111           | $4.3 \cdot 10^5$           | 3.8  | 1.2  | 89                                      | 574  |
| SC349  | $6.7 \pm 0.7$                                      | 300      | 1.223                        | $2.9 \cdot 10^6$                        | 1.222           | $2.6 \cdot 10^6$           | 8.9  | 5.6  | 15                                      | 11   |
|        |  | 320      | 1.183                        | $1.7 \cdot 10^6$                        | 1.182           | $1.7 \cdot 10^6$           | 1.2  | 0.4  | 10                                      | 32   |
|        |  | 340      | 1.138                        | $1.3 \cdot 10^6$                        | 1.173           | $1.3 \cdot 10^6$           | 9.8  | 1.7  | 26                                      | 411  |

Also, it should be noted that the results confirm the trends revealed by the analysis of synthetic IV curves. In particular, the prediction accuracy decreases at  $T > 320$  K and iron concentrations close to the upper limit in the range ( $10^{13} \text{ cm}^{-3}$ ). These facts completely coincide with the data in Figures 4A and 7A, respectively. In addition, the sample's base doping level ( $N_B = 1.4 \cdot 10^{15} \text{ cm}^{-3}$ ) is not used in the training dataset but can be found in the d-varied dataset (see Supplementary Material). Table 5 shows that the prediction of  $\text{DNN}_{\text{FeFeB}}$  trained by a full dataset is better than in the case of learning only by a training dataset, especially for SC320 sample. This fact confirms the conclusion made in the previous section about the importance of DNN training with  $N_B$  values, which are expected to be the object of future research.

On the other hand, contrary to our expectations,  $\text{DNN}_{\text{FeFeB} - \text{Fe}}$  demonstrates worse performance than  $\text{DNN}_{\text{FeFeB}}$  in the majority case. The likely reasons are the following. First, the use of two ideality factor values makes the influence of simulation simplifications more significant (e.g., the effect of unaccounted processes that cause both shunt and series resistance). Second, to obtain a correct  $n_{\text{Fe}}$  is a more complicated experimental task than to determine  $n_{\text{Fe} - \text{FeB}}$ . For example, in our experiment it took about 100 s to obtain IV characteristics after intense illumination. This interval included the time required to set the temperature after illumination-induced heating and the time of measurement. According to previous studies,<sup>42,55</sup> the characteristic association time of FeB pairs at  $T = 340$  K and  $N_B = 1.4 \cdot 10^{15} \text{ cm}^{-3}$  is about 600 s. That is, despite the potentially higher accuracy of the  $\text{DNN}_{\text{FeFeB} - \text{Fe}}$  predictions (shown in the previous section), the practical application of this approach is more complicated.

On the whole, the results obtained for real SCs confirm the possibility to estimate iron contamination using the ideality factor.

Finally, we would like to suggest some speculations about the applicability of the trained DNNs to different SC structures. The speculations are based on assumption that the ideality factor distinguishes depletion-region recombination from most other sources of recombination.<sup>50,56</sup> Certainly, there are some deviations from this rule for real structures. For instance, our simulation reveals the  $n$  dependence on base thickness.<sup>52</sup> Nevertheless this dependence is weak, and the

ideality factor value is mainly determined by depletion-region recombination.

First of all, the DNNs applicability depends on the requirement for Shockley-Read-Hall recombination to be predominant. In case, if there are other mechanisms causing free carrier concentration to decrease, the models which diverge from the two-diode one are proposed (e.g., three-diode<sup>57,58</sup>). Moreover, the base must be doped by boron. For example, if SC is prepared from Si:Al wafer, the simulation model which is used for training dataset preparation must be modified: the parameters of  $\text{Fe}_i\text{Al}_s$  pair as well as the changes in defect distribution (Equation 9) should be taken into consideration. Finally, if another type of defect (in addition to iron-related deep levels) is present in the solar cell, which also induces intensive SRH recombination, the simulation model must be more complicated as well. The primary competitors of  $\text{Fe}_i\text{B}_s$  are boron-oxygen complexes<sup>59,60</sup> and oxide precipitates<sup>61,62</sup> in Cz-Si. So the development of the corresponding model can be our next step. To the point, it should be noted that a high  $n$  value can serve an indicator of another defect presence: in our simulation this value is  $n < 1.4$ . The absence of non-iron active defects may be the most limiting factor of the DNNs applicability; In particular, this confined the selection of SCs for our experimental verification of the proposed method.

Thus, the trained DNNs can be applied to BSF solar cells prepared from Si:B wafers. It should be noted that the modern technique of crystal growth makes it possible to restrict oxygen concentration substantially even in solar grade Cz-Si. On the one hand, Al is used to produce the doped  $p^+$  region at the industrial level.<sup>23,24</sup> However, since a boron BSF is one of the promising techniques for achieving high quality back contact<sup>63,64</sup> therefore the  $p^+$  layer, which is doped by boron, was under our consideration. On the other hand, the probable  $p^+$ -layer influences this process mostly via the electric field. Therefore, the kind of doping atom in  $p^+$ -layer is not very important for simulation, and in our opinion, the DNNs is applicable for Al BSF cell as well. Besides, the recombination in the rear surface region is not crucially important for estimating the ideality factor. The wake aforesaid allows us to make a conclusion that the trained DNN can be applied to those PERC solar cell in which (i) the base is boron-doped; (ii) the iron-related deep levels are the main cause of defect-assisted recombination.

## 5 | CONCLUSION AND OUTLOOK

In this paper, we determined iron concentration in silicon BSF solar cells from the ideality factor value and systematically studied the performance of deep learning for the indicated task. It was the first attempt to use deep learning for retrieving deep level parameters from the current-voltage curve. In the model study, we performed simulation in order to obtain a training labeled dataset and test labeled datasets. In the end, DNN was trial-tested by using the parameters of actual solar cells. Our results showed the DNN ability to predict iron concentration by ideality factor, thickness and doping level of SC base as well as temperature. For synthetic datasets the MSRE was as small as 0.005. Our simulation shows the prospects for applying the ideality factor of two values (for structure with Fe<sub>i</sub> only as well as with Fe<sub>i</sub>B<sub>s</sub> and Fe<sub>i</sub> coexistence) in order to upgrade prediction accuracy. At the same time, the practical application of this approach demonstrated difficulties in obtaining correct data. It was important to train the DNN with boron concentration values, which agreed with the doping level of the structures under study. Moreover, the increase in iron or boron concentration, as well as temperature decrease, resulted in smaller prediction errors.

The proposed approach uses a simple and widely applied setup and does not take much time. Therefore, it could be easily integrated into the manufacturing environment. It should be noted, however, that for our purposes the task was simplified. Nevertheless, we believe that this DNN approach can be further improved in two ways. The first is to refine labeled datasets by using 3D-simulators (e.g., SILVACO TCAD) or real IV measurements in a broad set of SCs. The second is to improve DNN operation, and fine-tuning seems to be most promising in this case. For example, innumerable input parameters can be multiplied and transformed into a picture so that the vision model (e.g., VGG16) could be applied.

## ACKNOWLEDGEMENT

This work was supported by National Research Foundation of Ukraine (project number 2020.02/0036)

## CONFLICT OF INTEREST

The authors declare that they have no known competing financial interests or personal relationships that could have appeared to influence the work reported in this paper.

## DATA AVAILABILITY STATEMENT

The simulated IV characteristics,  $n_{Fe}$  and  $n_{Fe-FeB}$  values, and trained DNNs are available at <https://github.com/olegolik/IVcharacteristics.git>.

## ORCID

Oleg Olikh  <https://orcid.org/0000-0003-0633-5429>

Oleg Lozitsky  <https://orcid.org/0000-0002-6872-6655>

Oleksii Zavhorodnii  <https://orcid.org/0000-0001-8080-7661>

## REFERENCES

1. Claeys C, Simoen E. *Metal Impurities in Silicon- and Germanium-based Technologies: Origin, Characterization, Control, and Device Impact*, Springer Series in Materials Science, vol. 270. Berlin/New York: Springer International Publishing; 2018.
2. Schmidt J. Effect of dissociation of iron-boron pairs in crystalline silicon on solar cell properties. *Prog Photovolt Res Appl*. 2005;13(4):325-331.
3. Schubert MC, Padilla M, Michl B, et al. Iron related solar cell instability: imaging analysis and impact on cell performance. *Sol Energy Mater Sol Cells*. 2015;138:96-101.
4. Zhu H, Yu X, Zhu X, Wu Y, He J, Vanhellemont J, Yang D. Low temperature iron gettering by grown-in defects in p-type Czochralski silicon. *Superlattices Microstruct*. 2016;99:192-196.
5. Kurchin RC, Poindexter JR, Vähänissi V, Savin H, del Cañizo C, Buonassisi T. How much physics is in a current-voltage curve? Inferring defect properties from photovoltaic device measurements. *IEEE J Photovolt*. 2020;10(6):1532-1537.
6. Peaker AR, Markevich VP, Coutinho J. Tutorial: junction spectroscopy techniques and deep-level defects in semiconductors. *J Appl Phys*. 2018;123(16):161559.
7. Schroder DK. *Semiconductor Material and Device Characterization*. 3rd ed. New Jersey: John Wiley & Sons; 2006.
8. Bulyarskiy SV, Lakalin AV, Saurov MA, Gusarov GG. The effect of vacancy-impurity complexes in silicon on the current-voltage characteristics of p-n junctions. *J Appl Phys*. 2020;128(15):155702.
9. Bulyarskiy SV. The effect of electron-phonon interaction on the formation of reverse currents of p-n-junctions of silicon-based power semiconductor devices. *Solid-State Electron*. 2019;160:107624.
10. Claeys C, Simoen E. Device performance as a metrology tool to detect metals in silicon. *Phys Status Solidi (a)*. 2019;216(17):1900126.
11. Simoen E, Claeys C, Vanhellemont J. Defect analysis in semiconductor materials based on p-n junction diode characteristics. *Defects and diffusion in semiconductors—an annual retrospective ix: Defect and Diffusion Forum Trans Tech Publications Ltd*; 2007:1-24.
12. Olikh OY. Relationship between the ideality factor and the iron concentration in silicon solar cells. *Superlattices Microstruct*. 2019;136:106309.
13. Calado P, Burkitt D, Yao J, et al. Identifying dominant recombination mechanisms in perovskite solar cells by measuring the transient ideality factor. *Phys Rev Appl*. 2019;11:44005.
14. Chen J, Zhu M, Lu X, Zou X. Electrical characterization of GaN Schottky barrier diode at cryogenic temperatures. *Appl Phys Lett*. 2020;116(6):62102.
15. Dalapati P, Manik NB, Basu AN. Analysis of the temperature dependence of diode ideality factor in InGaN-based UV-A light-emitting diode. *Semiconductors*. 2020;54(10):1284-1289.
16. Duan L, Yi H, Xu C, Upama MB, Mahmud MA, Wang D, Shabab FH, Uddin A. Relationship between the diode ideality factor and the carrier recombination resistance in organic solar cells. *IEEE J Photovolt*. 2018;8(6):1701-1709.
17. van der Heide ASH, Schonecker A, Bultman JH, Sinke WC. Explanation of high solar cell diode factors by nonuniform contact resistance. *Prog Photovolt Res Appl*. 2005;13(1):3-16.
18. Carleo G, Cirac I, Cranmer K, et al. Machine learning and the physical sciences. *Rev Mod Phys*. 2019;91:45002.
19. Ju S, Shimizu S, Shiomi J. Designing thermal functional materials by coupling thermal transport calculations and machine learning. *J Appl Phys*. 2020;128(16):161102.
20. Rodrigues S, Ramos HG, Morgado-Dias F. Machine learning pv system performance analyser. *Prog Photovoltaics Res Appl*. 2018;26(8):675-687.
21. Jean J, Brown PR, Jaffe RL, Buonassisi T, Bulović V. Pathways for solar photovoltaics. *Energy Environ Sci*. 2015;8(4):1200-1219.
22. Ajayan J, Nirmal D, Mohankumar P, Saravanan M, Jagadeesh M, Arivazhagan L. A review of photovoltaic performance of organic/inorganic solar cells for future renewable and sustainable energy technologies. *Superlattices Microstruct*. 2020;143:106549.

23. Green MA. Photovoltaic technology and visions for the future. *Prog Energy*. 2019;1(1):13001.
24. Wilson GM, Al-Jassim M, Metzger WK, et al. The 2020 photovoltaic technologies roadmap. *J Phys D Appl Phys*. 2020;53(49):493001.
25. Burgelman M, Nollet P, Degraeve S. Modelling polycrystalline semiconductor solar cells. *Thin Solid Films*. 2000;361–362:527–532.
26. Decock K, Khelifi S, Burgelman M. Modelling multivalent defects in thin film solar cells. *Thin Solid Films*. 2011;519(21):7481–7484.
27. Boubakeur M, Aissat A, Ben Arbia M, Maaref H, Vilecot JP. Enhancement of the efficiency of ultra-thin CIGS/Si structure for solar cell applications. *Superlattices Microstruct*. 2020;138:106377.
28. Cappelletti MA, Casas GA, Cédola AP, y Blancá ELP, Soucase BM. Study of the reverse saturation current and series resistance of p–p–n perovskite solar cells using the single and double-diode models. *Superlattices Microstruct*. 2018;123:338–348.
29. Casas GA, Cappelletti MA, Cédola AP, Soucase BM, Peltzer y Blancá EL. Analysis of the power conversion efficiency of perovskite solar cells with different materials as hole-transport layer by numerical simulations. *Superlattices Microstruct*. 2017;107:136–143.
30. Hamache A, Sengouga N, Meftah A, Henini M. Modeling the effect of 1 MeV electron irradiation on the performance of  $n^+ - p - p^+$  silicon space solar cells. *Radiat Phys Chem*. 2016;123:103–108.
31. Hu ET, Yue GQ, Zhang RJ, Zheng YX, Chen LY, Wang SY. Numerical simulations of multilevel impurity photovoltaic effect in the sulfur doped crystalline silicon. *Renew Energy*. 2015;77:442–446.
32. Kim K, Gwak J, Ahn SK, et al. Simulations of chalcopyrite/c-Si tandem cells using scaps-1d. *Sol Energy*. 2017;145:52–58.
33. Pässler R. Dispersion-related description of temperature dependencies of band gaps in semiconductors. *Phys Rev B*. 2002;66:85201.
34. Yan D, Cuevas A. Empirical determination of the energy band gap narrowing in  $p^+$  silicon heavily doped with boron. *J Appl Phys*. 2014;116(19):194505.
35. Green MA. Intrinsic concentration, effective densities of states, and effective mass in silicon. *J Appl Phys*. 1990;67(6):2944–2954.
36. Couderc R, Amara M, Lemiti M. Reassessment of the intrinsic carrier density temperature dependence in crystalline silicon. *J Appl Phys*. 2014;115(9):93705.
37. Klaassen DBM. A unified mobility model for device simulation—I. model equations and concentration dependence. *Solid-State Electron*. 1992;35(7):953–959.
38. O'Mara WC, Herring RB, Hant LP. *Handbook of Semiconductor Silicon Technology*. New Jersey, USA: Noyes Publications; 1990.
39. Altermatt PP, Schmidt J, Heiser G, Aberle AG. Assessment and parameterisation of Coulomb-enhanced Auger recombination coefficients in lowly injected crystalline silicon. *J Appl Phys*. 1997;82(10):4938–4944. <https://doi.org/10.1063/1.366360>
40. Nguyen HT, Baker-Finch SC, Macdonald D. Temperature dependence of the radiative recombination coefficient in crystalline silicon from spectral photoluminescence. *Appl Phys Lett*. 2014;104(11):112105. <https://doi.org/10.1063/1.4869295>
41. Macdonald D, Roth T, Deenapanray PNK, Bothe K, Pohl P, Schmidt J. Formation rates of iron-acceptor pairs in crystalline silicon. *J Appl Phys*. 2005;98(8):83509.
42. Möller C, Bartel T, Gibaja F, Lauer K. Iron-boron pairing kinetics in illuminated p-type and in boron/phosphorus co-doped n-type silicon. *J Appl Phys*. 2014;116(2):24503.
43. Tan J, Macdonald D, Rougieux F, Cuevas A. Accurate measurement of the formation rate of iron–boron pairs in silicon. *Semicond Sci Technol*. 2011;26(5):55019.
44. Wijaranakula W. The reaction kinetics of iron–boron pair formation and dissociation in p-type silicon. *J Electrochem Soc*. 1993;140(1):275–281.
45. Murphy JD, Bothe K, Olmo M, Voronkov VV, Falster RJ. The effect of oxide precipitates on minority carrier lifetime in p-type silicon. *J Appl Phys*. 2011;110(5):53713.
46. Zoth G, Bergholz W. A fast, preperetion-free method to detect iron in silicon. *J Appl Phys*. 1990;67(11):6764–6771.
47. Geerligs LJ, Macdonald D. Dynamics of light-induced FeB pair dissociation in crystalline silicon. *Appl Phys Lett*. 2004;85(22):5227–5229.
48. Rougieux FE, Sun C, Macdonald D. Determining the charge states and capture mechanisms of defects in silicon through accurate recombination analyses: A review. *Sol Energy Mater Sol Cells*. 2018;187:263–272.
49. Istratov AA, Hieslmair H, Weber ER. Iron and its complexes in silicon. *Appl Phys A Mater Sci Process*. 1999;69(1):13–44.
50. Breitenstein O. Understanding the current-voltage characteristics of industrial crystalline silicon solar cells by considering inhomogeneous current distributions. *Opto-Electron Rev*. 2013;21(3):259–282.
51. Yu K, Liang JJ, Qu BY, Chen X, Wang H. Parameters identification of photovoltaic models using an improved JAYA optimization algorithm. *Energy Convers Manag*. 2017;150:742–753.
52. Olikh OY, Zavhorodnii OV. Modeling of ideality factor value in  $n^+ - p - p^+$ -si structure. *J Phys Stud*. 2020;24(4):4701.
53. Chollet F. *Deep learning with python*. 2nd ed.: Manning; 2017.
54. Olikh O, Kostilyov V, Vlasuk V, Korkishko R, Olikh Y, Chupryna R. Features of FeB pair light-induced dissociation and repair in silicon  $n^+ - p - p^+$  structures under ultrasound loading. *J Appl Phys*. 2021;130(23):235703. <https://doi.org/10.1063/5.0073135>
55. Khelifati N, Laine HS, Vähänissi V, Savin H, Bouamama FZ, Bouhafs D. Dissociation and formation kinetics of iron–boron pairs in silicon after phosphorus implantation gettering. *Phys Status Solidi A*. 2019;216(17):1900253.
56. McIntosh K, Altermatt P, Heiser G. Depletion–region recombination in silicon solar cells. when does  $mdr = 2$ ? *16th european photovoltaic solar energy conference: Proceedings of the international conference and exhibition*: Publisher:James and James (Science Publishers) Ltd; 2000:250–253.
57. Hallam BJ, Hamer PG, Bonilla RS, Wenham SR, Wilshaw PR. Method of extracting solar cell parameters from derivatives of dark I–V curves. *IEEE J Photovoltaics*. 2017;7(5):1304–1312.
58. Shah JM, Li Y-L, Gessmann T, Schubert EF. Experimental analysis and theoretical model for anomalously high ideality factors ( $n \gg 2.0$ ) in AlGaIn/GaN p–n junction diodes. *J Appl Phys*. 2003;94(4):2627–2630.
59. Lindroos J, Savin H. Review of light-induced degradation in crystalline silicon solar cells. *Sol Energy Mater Sol Cells*. 2016;147:115–126.
60. Niewelt T, Schön J, Warta W, Glunz SW, Schubert MC. Degradation of crystalline silicon due to boron–oxygen defects. *IEEE J Photovoltaics*. 2017;7(1):383–398.
61. Chen L, Yu X, Chen P, Wang P, Gu X, Lu J, Yang D. Effect of oxygen precipitation on the performance of Czochralski silicon solar cells. *Sol Energy Mater Sol Cells*. 2011;95(11):3148–3151.
62. Murphy JD, McGuire JD, Bothe K, Voronkov VV, Falster RJ. Minority carrier lifetime in silicon photovoltaics: the effect of oxygen precipitation. *Sol Energy Mater Sol Cells*. 2014;120:402–411.
63. Du G, Chen B, Chen N, Hu R. Efficient boron doping in the back surface field of crystalline silicon solar cells via alloyed-aluminum–boron paste. *IEEE Electron Device Lett*. 2012;33(4):573–575.

64. Kim DS, Nakayashiki K, Rounsaville B, Meemongkolkat V, Rohatgi A. Silicon solar cells with boron back surface field formed by using boric acid. In: 22th European photovoltaic solar energy conference: Proceedings of the international conference and exhibition; 2007: 1730-1733.

#### SUPPORTING INFORMATION

Additional supporting information may be found in the online version of the article at the publisher's website.

**How to cite this article:** Olikh O, Lozitsky O, Zavorodnii O. Estimation for iron contamination in Si solar cell by ideality factor: Deep neural network approach. *Prog Photovolt Res Appl*. 2022;1-13. doi:10.1002/pip.3539